

determined from the standard error of the measurements in that data set (17). At an axial temperature $T_Z \approx 7 \mu\text{K}$, the collisional shift in our 2D lattice clock was measured to be $5.6 (\pm 1.3) \times 10^{-17}$ in fractional units, with $\sqrt{\chi^2_{\text{red}}} \approx 0.84$. At a lower T_Z of $3.5 \mu\text{K}$, the collisional shift is reduced to $0.5 (\pm 1.7) \times 10^{-17}$, with $\sqrt{\chi^2_{\text{red}}} \approx 0.73$ (Fig. 4C). The corresponding Allan deviations of both data sets are shown in Fig. 4, B and D.

Relative to previous measurements of collisional shifts in a 1D optical lattice (8, 10), the atomic density in our 2D lattice is an order of magnitude higher. Hence, given a similar level of excitation inhomogeneity, if the collisional shift in a 2D lattice were not suppressed, we would expect a larger shift than seen in earlier results, even after accounting for the fact that only 20 to 30% of lattice sites are contributing.

The advance presented here removes an important obstacle to further increasing the precision and accuracy of neutral atom–based optical clocks. Increasing the number of atoms loaded into our 2D lattice system will enable us to improve the stability of our clock without imposing an onerous systematic effect. As clock lasers become more stable, we will increase the duration of the Rabi interrogation pulse, thus decreasing the Rabi frequency,

further reducing the collisional shift systematic well into the 10^{-18} domain. This, together with the fact that in the strongly interacting regime the collisional shift will remain suppressed (25) as more atoms are loaded into individual lattice sites, should enable neutral atom clocks to operate with the large sample sizes needed to achieve the highest possible stability.

References and Notes

1. S. Gupta *et al.*, *Science* **300**, 1723 (2003).
2. M. Punk, W. Zwerger, *Phys. Rev. Lett.* **99**, 170404 (2007).
3. G. Baym, C. J. Pethick, Z. Yu, M. W. Zwierlein, *Phys. Rev. Lett.* **99**, 190407 (2007).
4. M. Girardeau, *J. Math. Phys.* **1**, 516 (1960).
5. T. Kinoshita, T. Wenger, D. S. Weiss, *Science* **305**, 1125 (2004).
6. B. Paredes *et al.*, *Nature* **429**, 277 (2004).
7. E. Haller *et al.*, *Science* **325**, 1224 (2009).
8. A. D. Ludlow *et al.*, *Science* **319**, 1805 (2008).
9. M. D. Swallows *et al.*, *IEEE Trans. Ultrason. Ferroelectr. Freq. Control* **57**, 574 (2010).
10. G. K. Campbell *et al.*, *Science* **324**, 360 (2009).
11. N. D. Lemke *et al.*, *Phys. Rev. Lett.* **103**, 063001 (2009).
12. K. Gibble, *Phys. Rev. Lett.* **103**, 113202 (2009).
13. A. M. Rey, A. V. Gorshkov, C. Rubbo, *Phys. Rev. Lett.* **103**, 260402 (2009).
14. Z. Yu, C. J. Pethick, *Phys. Rev. Lett.* **104**, 010801 (2010).
15. M. M. Boyd *et al.*, *Phys. Rev. A* **76**, 022510 (2007).
16. T. Akatsuka, M. Takamoto, H. Katori, *Nat. Phys.* **4**, 954 (2008).
17. See supporting material on Science Online.
18. M. Saffman, T. G. Walker, K. Molmer, *Rev. Mod. Phys.* **82**, 2313 (2010).
19. G. K. Campbell *et al.*, *Metrologia* **45**, 539 (2008).
20. J. Ye, H. J. Kimble, H. Katori, *Science* **320**, 1734 (2008).
21. S. Blatt *et al.*, *Phys. Rev. A* **80**, 052703 (2009).
22. A. D. Ludlow *et al.*, *Opt. Lett.* **32**, 641 (2007).
23. M. M. Boyd *et al.*, *Phys. Rev. Lett.* **98**, 083002 (2007).
24. W. B. Dress, P. D. Miller, J. M. Pendlebury, P. Perrin, N. F. Ramsey, *Phys. Rev. D* **15**, 9 (1977).
25. We recently became aware of a conference proceedings report that contains a brief discussion on suppression of collisional shifts under strong interactions (26).
26. K. Gibble, www.ieee-uffc.org/main/publications/fcs/toc.asp?year=2010.
27. We thank C. Benko for technical assistance, and A. D. Ludlow and A. Gorshkov for useful discussions. Supported by a National Research Council postdoctoral fellowship (M.D.S.), a National Defense Science and Engineering Graduate fellowship (M.B.), and a grant from the Army Research Office with funding from the Defense Advanced Research Projects Agency OLE program, the National Institute of Standards and Technology, the NSF Physics Frontier Center at JILA, and the Air Force Office of Scientific Research.

Supporting Online Material

www.sciencemag.org/cgi/content/full/science.1196442/DC1
Materials and Methods
Figs. S1 to S4
References

12 August 2010; accepted 20 January 2011
Published online 3 February 2011;
10.1126/science.1196442

Direct Measurement of Long-Range Third-Order Coherence in Bose-Einstein Condensates

S. S. Hodgman, R. G. Dall, A. G. Manning, K. G. H. Baldwin, A. G. Truscott*

A major advance in understanding the behavior of light was to describe the coherence of a light source by using correlation functions that define the spatio-temporal relationship between pairs and larger groups of photons. Correlations are also a fundamental property of matter. We performed simultaneous measurement of the second- and third-order correlation functions for atoms. Atom bunching in the arrival time for pairs and triplets of thermal atoms just above the Bose-Einstein condensation (BEC) temperature was observed. At lower temperatures, we demonstrated conclusively the long-range coherence of the BEC for correlation functions to third order, which supports the prediction that like coherent light, a BEC possesses long-range coherence to all orders.

The interchangeability of particle and wave-like behavior is fundamental to the quantum-mechanical description of light, but not until the seminal work of Glauber (1) was quantum theory used to provide a description of the coherence properties of photon statistics that moves beyond classical theory. That work distinguishes between the classical, first-order coherence of the light intensity and the quantum coherence between n multiple photons (n th-order correlations); a perfectly coherent source exhibits coherence to all orders. For example, measurement of the ar-

rival time of individual photons at a detector enables the correlation between pairs (second-order), triplets (third-order), and higher-order groups of photons to be determined. An incoherent source of light will exhibit bosonic photon bunching—that is, an enhanced probability of pairs of photons arriving within an interval that defines the coherence time of the source. Such second-order correlations were first demonstrated in the famous Hanbury Brown and Twiss (HBT) experiment (2), a technique that was later applied in astronomy in the spatial domain to determine the angular size of stars (3). Conversely, a highly coherent light source such as a laser will exhibit no bunching, with a uniform arrival-time probability for pairs, triplets, and larger groupings of photons; this indicates long-range coherence to all orders in the corresponding (unity-value) correlation functions.

The same concepts can be applied to the quantum statistics of matter, with correlations demonstrated in systems ranging from nuclear collisions (4) to free electrons (5) to neutrons (6). In atomic physics, correlations can potentially be probed by using spin polarization spectroscopy (7, 8), spin-squeezing entanglement (9, 10), and interactions between atoms in single-occupancy optical lattices (11). Specifically, incoherent sources of bosonic atoms have also been shown to exhibit HBT-like (second-order) bunching behavior (12, 13), whereas incoherent fermionic sources exhibit anti-bunching (a reduced probability of particles being found close together) (14, 15) as a consequence of the Pauli exclusion principle. However, correlations higher than second order are often difficult to measure because the vast amounts of data require extensive data analysis resources. Correlations up to third order have been measured for exciton-polaritons (16) and to fourth order for photons (17).

First-order (18) and second-order correlations (12–15, 19–22) have been measured for atomic matter waves, and the effect of second- and third-order correlations on two-body (23) and three-body (24, 25) loss rates has been demonstrated. In order to prove that an atomic ensemble is completely quantum coherent, it is necessary to demonstrate coherence in the third (and subsequent) orders (1). Measurements of third- and higher-order correlations are also important in order to understand whether the interactions between atoms (not present for photons) affect the coherence of matter-wave sources, such as Bose-Einstein condensates (BECs). Intrinsically, higher-order (n body) correlation functions are a

Australian Research Council Centre of Excellence for Quantum Atom Optics, Research School of Physics and Engineering, Australian National University, Canberra, ACT 0200, Australia.

*To whom correspondence should be addressed. E-mail: andrew.truscott@anu.edu.au

more sensitive test of coherence because in an idealized system, for zero delay between arrival times the ratio of incoherent to coherent behavior scales as n factorial ($n!$) (1). Like the laser, a BEC is thought to exhibit a constant (unity) correlation function to all orders because it is described theoretically by a single macroscopic wave function that is characterized by long-range coherence.

We have achieved simultaneous second- and third-order correlation measurements through a combination of two key experimental factors: the single-atom detection properties of metastable helium atoms He^* [the metastable 2^3S_1 state has a lifetime of ~ 8000 s (26) and contains ~ 20 eV of internal energy, enabling high detection efficiencies (27)] and a new method for collecting a large

data set of correlation statistics from the atomic ensemble (28).

The principle of the experiment is shown in Fig. 1. An atomic cloud incident on the detector has both the position and arrival time recorded for each individual atom. The correlation function can then be determined for atom pairs (second order) and triplets (third order, shown enlarged) by measuring the delay time τ between atoms arriving within each analysis region.

An ensemble of $\sim 10^6$ He^* atoms (either a thermal cloud or atoms that have been cooled below the BEC critical temperature) are output-coupled from a bi-planar quadrupole Ioffe configuration (BiQUIC) (29) magnetic trap by using radio-frequency (RF) radiation to flip the spins of the atoms from the trapped $m_j = 1$ state to the field-insensitive $m_j = 0$ state, where m_F is the magnetic quantum number. The atoms then fall 848 mm under gravity for 416 ms onto an 80-mm-diameter microchannel plate detector (MCP), which measures their arrival time. The He^* ~ 20 eV internal energy releases electrons that are amplified by a voltage across the MCP to create an electron pulse on a separate delay line detector, which measures the spatial position in the horizontal plane.

In order to build a large statistical sample while not saturating the detector, a sequence of 30 RF pulses (each of 5 μs duration separated by

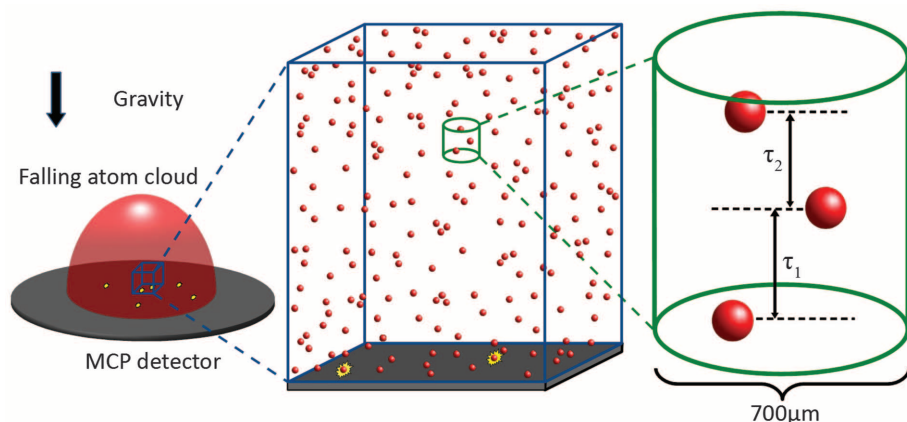


Fig. 1. Experimental setup: An ensemble of He^* atoms (red spheres) falls under gravity onto the MCP detector creating a series of detection events (yellow) separated in space and time. The middle inset (blue box) shows the arrival of the atomic ensemble in more detail, whereas the right-hand inset (green cylinder) shows the arrival of a triplet of atoms within our analysis region. The third-order correlation function characterizes the arrival time differences τ_1 and τ_2 between the three atoms.

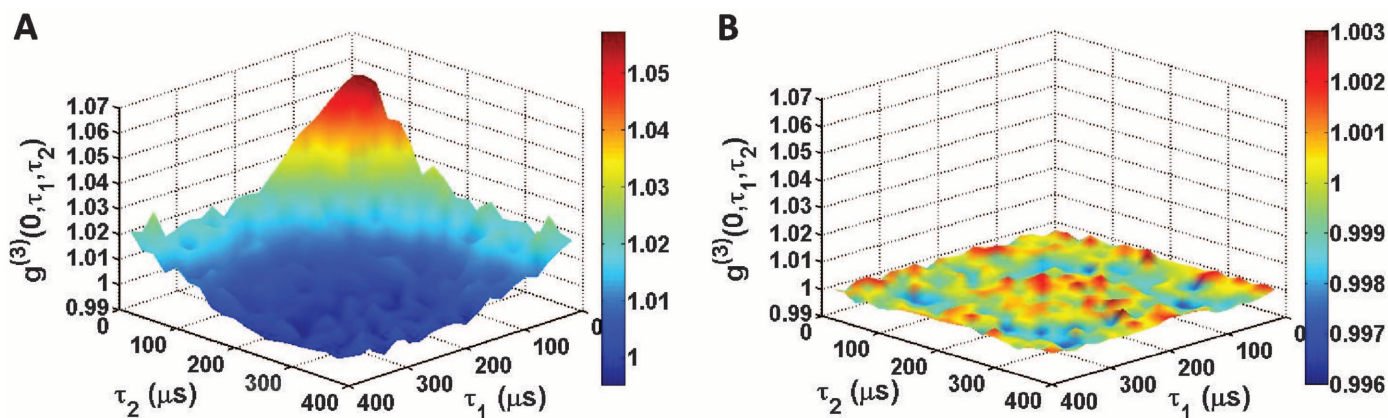


Fig. 2. Normalized third-order correlation functions $g^{(3)}(0, \tau_1, \tau_2)$ for (A) ensembles of thermal atoms and (B) the BEC.

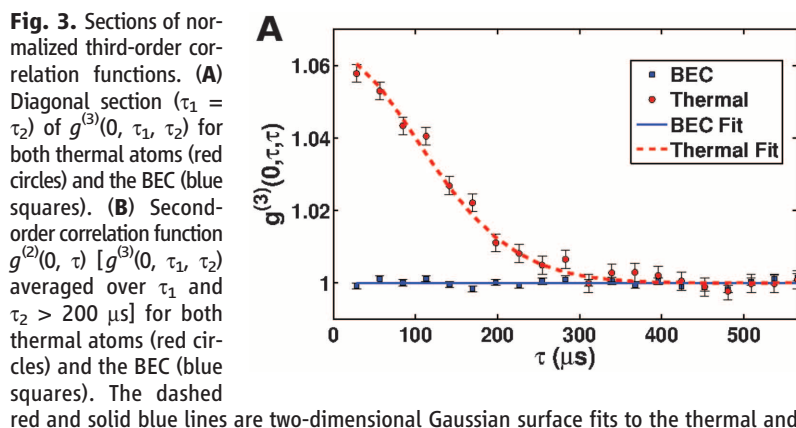


Fig. 3. Sections of normalized third-order correlation functions. (A) Diagonal section ($\tau_1 = \tau_2$) of $g^{(3)}(0, \tau_1, \tau_2)$ for both thermal atoms (red circles) and the BEC (blue squares). (B) Second-order correlation function $g^{(2)}(0, \tau)$ [$g^{(3)}(0, \tau_1, \tau_2)$ averaged over τ_1 and $\tau_2 > 200$ μs] for both thermal atoms (red circles) and the BEC (blue squares). The dashed red and solid blue lines are two-dimensional Gaussian surface fits to the thermal and BEC data in Fig. 2, respectively.

Table 1. Comparison of experimental and model values for $g^{(2)}(0, \tau)$ and $g^{(3)}(0, \tau_1, \tau_2)$ with their respective uncertainties.

	Experiment	Theory
$g^{(2)}(0, \tau)$ max.	1.022(2)	1.025(5)
$g^{(2)}(0, \tau)$ width (μ s)	90(10)	80(20)
$g^{(3)}(0, \tau_1, \tau_2)$ max.	1.061(6)	1.075(15)
$g^{(3)}(0, \tau_1, \tau_2)$ width (μ s)	120(10)	100(20)
$[g^{(3)}(0,0,0) - 1]/[g^{(2)}(0,0) - 1]$	2.8(3)	3.0(3)

29 ms) were used to spin-flip ~ 2 to 3% of the atoms per pulse into the untrapped state, allowing them to fall onto the detector. The atoms remaining at the end of the sequence are released by switching off the trap (28). The amplitude of the RF power is ramped over time so as to keep the detector flux approximately constant. In order to uniformly sample over the entire cloud, the RF pulse width was chosen so that the radiation has a Fourier-broadened frequency width much greater than both the kinetic energy spread of the thermal cloud (~ 30 kHz) and the chemical potential of the atomic interactions in the BEC (~ 8 kHz).

The unnormalized third-order correlation function $G^{(3)}(0, \tau_1, \tau_2)$ (with the first particle setting the time origin at $\tau = 0$) was then determined from the number of coincidence events with relative arrival times τ_1 and τ_2 (Fig. 1). For each detection event measured on the MCP, the difference in arrival times τ_1 of all particles within $700 \mu\text{m}$ were recorded. Each of these pairs was then checked to determine whether a third particle arrived within the same radius, in which case the time difference τ_2 between particles two and three was also recorded.

The normalized temporal correlation function $g^{(3)}(0, \tau_1, \tau_2)$ was then obtained by dividing by the local particle densities. This was achieved by averaging the individual particle number over the analysis region in the x - y plane and identifying that τ is related to z by the impact velocity of the falling particle. This yields the time-of-flight correlation function

$$g^{(3)}(0, \tau_1, \tau_2) = \frac{G^{(3)}(0, \tau_1, \tau_2)}{\rho(0)\rho(\tau_1)\rho(\tau_2)} \quad (1)$$

where $\rho(\tau)$ is the density at time τ after the first particle is measured. In the idealized case of unlimited detector resolution, for thermal atoms this yields an asymptotic value of 1 at very large delay times τ , with a peak value of $g^{(3)}(0, 0, 0) = 3!$ (that is, 6) at zero delay times; the width of the peak defines the correlation time for the atomic ensemble. In contrast, a pure BEC is predicted to have a uniform $g^{(3)}(0, \tau_1, \tau_2) = 1$ because of its long-range, higher-order coherence.

In Fig. 2A, we plot the measured third-order correlation function for thermal atoms just above the BEC transition temperature ($T_c \sim 1.0 \mu\text{K}$) and contrast it with the data for the almost pure condensate well below T_c (Fig. 2B). Because of the finite detector resolution and our binning method, $g^{(3)}(0, 0, 0)$ for thermal atoms is greatly reduced from the idealized case [supporting on-

line material (SOM) text]. Because large amounts of data are necessary for correlation measurements, the thermal atom data [$T = 1.3(2) \mu\text{K}$] was taken from 24,600 individual experimental cycles, whereas the BEC data (of higher density, yielding more triplet coincidence events) was taken from 3700 cycles. The experimental data represents the result of ~ 250 hours of full-time data acquisition, but the limiting factor on the amount of data taken was the time required to process the second- and third-order correlations, which took longer than the experiments.

Figure 3A shows the cross-section of the $g^{(3)}(0, \tau_1, \tau_2)$ data for $\tau_1 = \tau_2$, which highlights the atom-bunching peak in the third-order correlation function. The maximum value measured for the thermal atoms was 1.061(6) at $g^{(3)}(0, 0, 0)$. This is to be compared with the mean value measured for the BEC in Fig. 2B of 1.000(1); within the 0.1% statistical variation in the correlation measurements, the BEC is coherent for the third order in the correlation function.

The second-order correlation function $g^{(2)}(0, \tau)$ can be derived from $g^{(3)}(0, \tau_1, \tau_2)$ by averaging the data for values of τ_1 or τ_2 much larger than the coherence time $\tau_c \sim 90(10) \mu\text{s}$ because in the limit of $\tau_1, \tau_2 \gg \tau_c$, $g^{(3)}(0, \tau_1, \tau_2)$ approaches $g^{(2)}(0, \tau)$. A maximum atom-bunching enhancement of $g^{(2)}(0, 0) = 1.022(2)$ is achieved for the thermal atoms (Fig. 3B). The BEC correlation value (also shown) is unity within the experimental statistical variation, indicating long-range coherence of the condensate for the second-order correlation function as well. This is in line with the prediction that coherence in a high-order correlation function requires coherence for all lower orders (l).

In order to quantitatively account for our results, we have applied a theoretical approach similar to that of (30) [based on the work in (31)]. These theoretical studies assume an ideal gas model, which is applicable in our experiments because the particle spacing covers a large range of distances ($>100 \mu\text{m}$), all of which are much greater than the interparticle scattering length [$7.512(5) \text{ nm}$ (32)].

This distinguishes the present $g^{(3)}(0, \tau_1, \tau_2)$ measurements from the measurement of three-body loss rates (24, 25), which by definition probe a limited range of distances at small interparticle separations that are strongly influenced by the details of the interatomic potential (31, 33). In that regime, the factorial relationship breaks down as interactions dominate the behavior of the correlation functions. In-trap correlation mea-

surements [for example, using single-occupancy optical lattices (11)] even need to consider modification of the correlation function at interparticle separations of hundreds of nanometers (31). Another feature of in-trap measurements is that they are dominated by local coherence effects rather than measuring the long-range coherence, as demonstrated very recently for a one-dimensional quasicondensate (22).

We have circumvented this issue by releasing atoms from the trap and measuring the correlation function at large interparticle separations after time-of-flight expansion, enabling a complete determination of $g^{(3)}(0, \tau_1, \tau_2)$ over a wide region of phase space, unaffected by short-range interparticle interactions.

Our model takes into account the known detector spatial and temporal resolution ($\sim 150 \mu\text{m}$ and $\sim 2 \text{ ns}$, respectively), the bin size ($700 \mu\text{m}$), the local charge depletion around the $30\text{-}\mu\text{m}$ -diameter MCP pores, and the electronic dead time ($\sim 100 \text{ ns}$). The model contains no free parameters and is in excellent agreement with experiment within the combined uncertainties (Table 1). It reproduces both the measured amplitude and width of $g^{(2)}(0, \tau)$ and $g^{(3)}(0, \tau_1, \tau_2)$ as well as the dramatic reduction in bunching signal resulting from the finite resolution.

A key result of the simultaneous measurement of $g^{(2)}(0, \tau)$ and $g^{(3)}(0, \tau_1, \tau_2)$ is that it enables a direct determination of the relative behavior of the second- and third-order correlation functions. As indicated by the factorial relationship between the peak theoretical bunching values for $g^{(2)}(0, 0)$ and $g^{(3)}(0, 0, 0)$, this relative behavior is a more sensitive probe of the quantum statistical differences between thermal and condensate atoms than the absolute enhancement of the second-order bunching peak. The measured ratio of the bunching enhancements ($g^{(3)}(0, 0, 0) - 1$)/($g^{(2)}(0, 0) - 1$) is 2.8(3), compared with the measured absolute enhancement values for $g^{(2)}(0, 0)$ and $g^{(3)}(0, 0, 0)$ of a few percent. This ratio is in excellent agreement with the model value of 3.0(3), which is relatively insensitive to the range of experimental parameters used.

These measurements provide strong confirmation of the quantum theory of boson statistics first developed in (1), as well as the prediction that a BEC possesses long-range coherence of matter waves to all orders in the correlation functions, in direct analogy with the long-range coherence of laser light.

References and Notes

1. R. J. Glauber, *Phys. Rev.* **130**, 2529 (1963).
2. R. Hanbury Brown, R. Q. Twiss, *Nature* **177**, 27 (1956).
3. R. Hanbury Brown, R. Q. Twiss, *Nature* **178**, 1046 (1956).
4. G. Baym, *Acta Physica Polonica B* **29**, 1839 (1998).
5. H. Kiesel, A. Renz, F. Hasselbach, *Nature* **418**, 392 (2002).
6. M. Iannuzzi, A. Orecchini, F. Sacchetti, P. Facchi, S. Pascazio, *Phys. Rev. Lett.* **96**, 080402 (2006).
7. K. Eckert, L. Zawitkowski, A. Sanpera, M. Lewenstein, E. S. Polzik, *Phys. Rev. Lett.* **98**, 100404 (2007).
8. K. Eckert et al., *Nat. Phys.* **4**, 50 (2008).
9. J. K. Korbicz, J. I. Cirac, M. Lewenstein, *Phys. Rev. Lett.* **95**, 120502 (2005).

10. J. K. Korbicz *et al.*, *Phys. Rev. A* **74**, 052319 (2006).
11. S. Trotzky, Y.-A. Chen, U. Schnorrberger, P. Cheinet, I. Bloch, *Phys. Rev. Lett.* **105**, 265303 (2010).
12. M. Yasuda, F. Shimizu, *Phys. Rev. Lett.* **77**, 3090 (1996).
13. M. Schellekens *et al.*, *Science* **310**, 648 (2005).
14. T. Rom *et al.*, *Nature* **444**, 733 (2006).
15. T. Jelte *et al.*, *Nature* **445**, 402 (2007).
16. T. Horikiri *et al.*, *Phys. Rev. B* **81**, 033307 (2010).
17. M. Assmann, F. Veit, M. Bayer, M. van der Poel, J. M. Hvam, *Science* **325**, 297 (2009).
18. M. R. Andrews *et al.*, *Science* **275**, 637 (1997).
19. A. Öttl, S. Ritter, M. Köhl, T. Esslinger, *Phys. Rev. Lett.* **95**, 090404 (2005).
20. S. Fölling *et al.*, *Nature* **434**, 481 (2005).
21. M. Greiner, C. A. Regal, J. T. Stewart, D. S. Jin, *Phys. Rev. Lett.* **94**, 110401 (2005).
22. S. Manz *et al.*, *Phys. Rev. A* **81**, 031610 (2010).
23. T. Kinoshita, T. R. Wenger, D. S. Weiss, *Phys. Rev. Lett.* **95**, 190406 (2005).
24. E. A. Burt *et al.*, *Phys. Rev. Lett.* **79**, 337 (1997).
25. B. Laburthe Tolra *et al.*, *Phys. Rev. Lett.* **92**, 190401 (2004).
26. S. S. Hodgman *et al.*, *Phys. Rev. Lett.* **103**, 053002 (2009).
27. K. G. H. Baldwin, *Contemp. Phys.* **46**, 105 (2005).
28. A. G. Manning, S. S. Hodgman, R. G. Dall, M. T. Johansson, A. G. Truscott, *Opt. Express* **18**, 18712 (2010).
29. R. G. Dall, A. G. Truscott, *Opt. Commun.* **270**, 255 (2007).
30. J. V. Gomes *et al.*, *Phys. Rev. A* **74**, 053607 (2006).
31. M. Naraschewski, R. J. Glauber, *Phys. Rev. A* **59**, 4595 (1999).
32. S. Moal *et al.*, *Phys. Rev. Lett.* **96**, 023203 (2006).
33. P. Ziñ, M. Trippenbach, M. Gadjia, *Phys. Rev. A* **69**, 023614 (2004).
34. The authors would like to acknowledge the support of the Australian Research Council Centre of Excellence for Quantum-Atom Optics.

Supporting Online Material

www.sciencemag.org/cgi/content/full/331/6020/1046/DC1

SOM Text

References

30 September 2010; accepted 21 January 2011

10.1126/science.1198481

Synthesis, Structure, and Reactivity of an Iron(V) Nitride

Jeremiah J. Scepianiak,¹ Carola S. Vogel,² Marat M. Khusniyarov,² Frank W. Heinemann,² Karsten Meyer,^{2*} Jeremy M. Smith^{1*}

Despite being implicated as important intermediates, iron(V) compounds have proven very challenging to isolate and characterize. Here, we report the preparation of the iron(V) nitrido complex, $[\text{PhB}(\text{tBulm})_3\text{Fe}^{\text{V}}\equiv\text{N}]\text{BAR}_{\text{F}24}$ ($\text{PhB}(\text{tBulm})_3^- = \text{phenyltris}(3\text{-tert-butylimidazol-2-ylidene})\text{borato}$, $\text{BAR}_{\text{F}24} = \text{B}(3,5\text{-(CF}_3)_2\text{C}_6\text{H}_3)_4^-$), by one electron oxidation of the iron(IV) nitrido precursor. Single-crystal x-ray diffraction of the iron(V) complex reveals a four-coordinate metal ion with a terminal nitrido ligand. Mößbauer and electron paramagnetic resonance spectroscopic characterization, supported by electronic structure calculations, provide evidence for a d^3 iron(V) metal center in a low spin ($S = 1/2$) electron configuration. Low-temperature reaction of the iron(V) nitrido complex with water under reducing conditions leads to high yields of ammonia with concomitant formation of an iron(II) species.

High-valent iron species are proposed as active intermediates in the cycles of many important biocatalysts. Iron(IV) is the most readily accessible high oxidation state, although iron(V) has also been shown as a key intermediate in some nonheme dioxygenases (1). Structural and spectroscopic precedent for these intermediates has often come from studies of well-defined model complexes. For example, the iron(IV) oxo moiety, which has long been known to be at the catalytic centers of oxygenases (2), was first crystallographically characterized in an octahedral iron complex of an *N*-methylated 1,4,8,11-tetraazacyclotetradecane (cyclam) macrocycle (3). Similar cyclam derivatives have also allowed for the preparation and detailed spectroscopic characterization of octahedral Fe(V) (4) and Fe(VI) (5) nitrido complexes, but the structural characterization and reactivity of these fleeting intermediates, which are usually studied at low temperatures in frozen matrices, remain elusive.

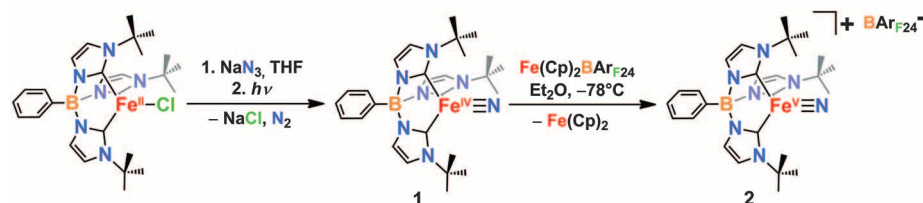
Iron nitrides have also been proposed to be key intermediates in the industrial (Haber-Bosch) (6) and biological (nitrogenase) (7, 8) synthesis of ammonia. Whereas iron-bound “surface nitride”

species are observed on the catalyst surface in the Haber-Bosch process (9), recent x-ray diffraction studies on nitrogenase suggest an interstitial atom in the center of the iron-sulfur cluster of the FeMo cofactor (10). Although it is tempting to suggest a nitride anion at the site of biological nitrogen reduction, the nature of this atom is controversial and still under debate (11, 12). Accordingly, the synthesis and characterization of model complexes is critical to delineating the reactivity of iron nitrides and their possible role in ammonia synthesis. In addition to the molecular and electronic structural insight provided by complexes that stabilize the $[\text{Fe}\equiv\text{N}]$ unit, their reactivity will also affect our understanding of both biological and industrial NH_3 syntheses.

Thermally stable, four-coordinate iron(IV) nitrido complexes were first prepared with tripodal tris(phosphino)borate supporting ligands, although these compounds could not be isolated in the solid state (13). Using ligands that are structurally and electronically related to

tris(phosphino)borates, we have recently reported the molecular and electronic structures, as well as preliminary reactivity, of low-coordinate Fe(IV) complexes that contain the $[\text{Fe}\equiv\text{N}]$ functionality (14, 15). We now report the synthesis of a four-coordinate iron(V) nitrido complex supported by a tripodal N-heterocyclic carbene (NHC) ligand. The complex has been characterized by single-crystal x-ray diffraction (XRD), Mößbauer, and electron paramagnetic resonance (EPR) spectroscopies as well as density functional theory (DFT) calculations. The enhanced reactivity of this complex is evident from a low-temperature hydrolysis reaction, which gives small amounts of ammonia, in contrast to the related iron(IV) nitrido complex, which is unreactive to water. Substantially higher yields of ammonia are obtained when the hydrolysis is conducted under reducing conditions, where water and the reductant provide three hydrogen atom equivalents. This reaction is reminiscent of the chemistry of nitrogenase, in which water is the ultimate source of protons in the synthesis of ammonia.

Some of us recently reported the synthesis and structure of the four-coordinate nitrido complex $[\text{PhB}(\text{tBulm})_3\text{Fe}^{\text{IV}}\equiv\text{N}]$ (**1**), where $\text{PhB}(\text{tBulm})_3^-$ is the phenyltris(3-*tert*-butylimidazol-2-ylidene) borato ligand (15). The Mößbauer spectrum of **1** (fig. S1) confirms the oxidation state assignment, with a negative isomer shift ($\delta = -0.28(1)$ mm s^{-1}) and large quadrupole splitting ($|\Delta E_Q| = 6.23(1)$ mm s^{-1}) similar to other iron(IV) nitrido complexes. At slow scan rates, the cyclic voltammogram of complex **1** (fig. S3) features a quasi-reversible oxidative wave that becomes fully reversible when the scan rate is increased ($E_{1/2} = -0.53$ V versus the ferrocene/ferrocenium couple in tetrahydrofuran solvent with 0.4 M tetrabutylammonium hexafluorophosphate electrolyte). The reversibility of the $\text{Fe}^{\text{V}}/\text{Fe}^{\text{IV}}$ redox couple at faster



Scheme 1. Formation of Fe(V) nitride **2**.

¹Department of Chemistry and Biochemistry, MSC 3C, New Mexico State University, Las Cruces, NM 88003, USA. ²Department of Chemistry and Pharmacy, Friedrich-Alexander-University Erlangen-Nuremberg, Egerlandstrasse 1, 91058 Erlangen, Germany.

*To whom correspondence should be addressed. E-mail: KMeyer@chemie.uni-erlangen.de (K.M.); jesmith@nmsu.edu (J.M.S.)

Direct Measurement of Long-Range Third-Order Coherence in Bose-Einstein Condensates

S. S. Hodgman, R. G. Dall, A. G. Manning, K. G. H. Baldwin, and A. G. Truscott

Science, 331 (6020), • DOI: 10.1126/science.1198481

View the article online

<https://www.science.org/doi/10.1126/science.1198481>

Permissions

<https://www.science.org/help/reprints-and-permissions>